Mechanism and Machine Theory 168 (2022) 104586

Contents lists available at ScienceDirect

Mechanism and Machine Theory

journal homepage: www.elsevier.com/locate/mechmt

Dynamics modeling and shift control of a novel spring-based synchronizer for electric vehicles

Yiwei Wang [a], Jinglai Wu [b,*], Nong Zhang [a], Wenwei Mo [b,*]

[a] Automotive Engineering Research Institute, Hefei University of Technology, Anhui, China
[b] School of Mechanical Science and Engineering, Huazhong University of Science and Technology, Hubei, China

ARTICLE INFO

Keywords:
Electric vehicle
Spring-based synchronizer
Engaging time
Vehicle jerk
Shift force control

ABSTRACT

This paper investigates the gearshift transient response and the shift control of a new spring-based synchronizer used in the automated manual transmission (AMT) for electric vehicles (EVs). The spring-based synchronizer uses torque spring to provide a torque to synchronize the speed difference between the target gear and the shaft, which reduces the wear caused by friction in traditional synchronizer, as well as decreases the engaging time and the vehicle jerk. The dynamics model of a two-speed AMT in EV equipped with the spring-based synchronizer is built in AMESim software, and the shift control model is established in MATLAB/Simulink environment. The simulation results of the dynamics model demonstrate that the spring-based synchronizer reduces the engaging time and the vehicle jerk compared to the traditional synchronizer. Furthermore, the influences of the motor inertia, speed difference, spring stiffness and shift force on the engaging time and vehicle jerk are quantitatively analyzed. Finally, several control strategies of shift force are proposed, including the single-closed loop PI position control, dual-closed loop PI control, and dual-closed loop fuzzy PI control, which further reduce the vehicle jerk.

1. Introduction

As the global issues of nonrenewable fuel shortage and environmental degradation are becoming serious, EVs have attracted worldwide attention due to their unique advantages, such as high efficiency, energy saving, zero missions and low noise [1–3]. Nowadays, most EVs are equipped with the single-speed transmission due to its low manufacturing cost, compact structure and small size [4–6]. However, the single-speed gearbox has to trade off the vehicle dynamic and economic performance [7]. The high-power EM is used in EVs to achieve the required dynamic performance, which increase the cost of EM. Since two-speed gearbox has the potential to save energy and improve dynamic performance, its application in EVs has received increasing attention [8–10]. Considering the simple configuration and high efficiency of AMT, the two-speed AMT will be more and more widely used in EVs [11]. In EVs, since the EM has extraordinary speed control characteristics and different working modes, including torque mode, speed mode and free mode, it can actively reduce the speed difference between the target gear and the shaft [12]. Hence, the clutch is usually canceled in EVs, and the EM is directly connected to the driveline, leading to a much higher equivalent rotary inertia on the target gear, and consequently greater shift shock or longer duration of speed synchronization for traditional synchronizers [13]. Furthermore, the traditional

This paper is submitted for possible publication in Mechanism and Machine Theory. It has not been previously published, is not currently submitted for review to any other journals, and will not be submitted elsewhere during the peer review.

* Corresponding authors.
E-mail addresses: wjlhust@163.com (J. Wu), mww.gdut@163.com (W. Mo).

https://doi.org/10.1016/j.mechmachtheory.2021.104586
Received 22 September 2021; Accepted 10 October 2021
Available online 21 October 2021
0094-114X/© 2021 Elsevier Ltd. All rights reserved.

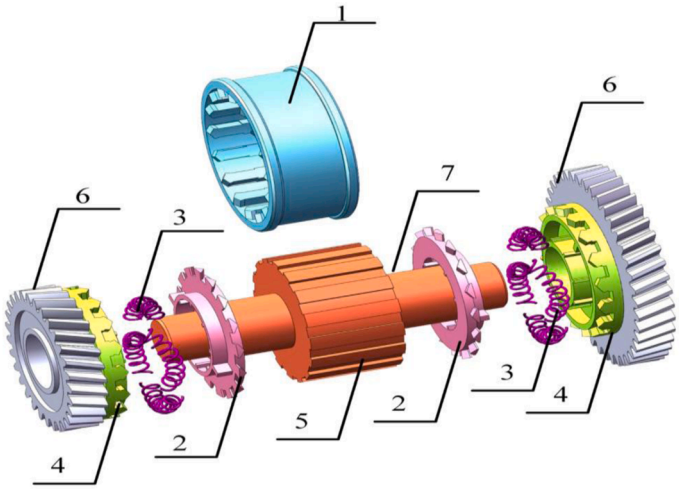

1. Sleeve; 2. Guide ring; 3. Torque spring; 4. Dog gear; 5. Hub; 6. Constant mesh gear; 7. Output shaft

Fig. 1. Overall structure diagram of spring-based synchronizer. 1. Sleeve; 2. Guide ring; 3. Torque spring; 4. Dog gear; 5. Hub; 6. Constant mesh gear; 7. Output shaft.

synchronizer depends on the friction to synchronize the speed difference [2]. As a result, the issues of energy dissipation in the form of heat energy as well as wear caused in the phase of speed synchronization will be inevitable, resulting in low shift efficiency or even the failure of engagement or damage of synchronizer. Secondly, relatively high shift force is required for the traditional synchronizer to ensure that the friction torque is large enough to reduce the synchronization time and to separate the friction ring from the target gear after the speed synchronization, leading to shift shock and high-power demand for gearshift electric motor. Therefore, in order to improve shift quality and efficiency of transmission, it is necessary to make innovations in the traditional synchronization mechanism.

In addition, the clutchless AMT also suffer poor shift quality due to the power interruption [14,15]. Hence, it is urgent to improve performance of synchronizer to reduce the duration of power interruption and improve the shifting quality. At present, there has been extensive research focused on how to improve the performance of synchronizer [16,17]. Sandooja proposed a position and force switch control scheme for AMT gear meshing to reduce the shift shock [18]. A double indexing synchronizer was proposed by Chen and Tian [19], aiming to increase the capacity of cone-type synchronizer. This improved synchronizer does not need to increase the gear ratio or use multi-cone synchronizer, but only needs a small modification to the traditional single-cone synchronizer, which can increase the capacity of the traditional synchronizer by 30%. A hybrid model of AMT traditional synchronizer is proposed in [20], to study the influence of shift force and the interaction between sleeve and friction ring or idle gear on meshing performance. Furthermore, the study conducted by Li et al. [21] demonstrated that the precise position control of shift actuator is significant for reducing the duration of gear change. Then a robust position control method was proposed, and the effectiveness of the control scheme was verified by experiments.

Yu et al. [22] designed a new electromagnetic shifting system to reduce the shifting load and improve the shift quality. In order to improve the system's robustness and realize precise displacement control, an active disturbance rejection controller was designed. The experimental results demonstrated that the shift force and the vehicle jerk can be reduced greatly. Wu et al. [23] studied the shift process without clutch by building a model of single-shaft parallel hybrid electric vehicle equipped with AMT. Their research will help to find out the phenomenon of frequent failure of traditional synchronizer. Yu and Yow [24,25] applied sliding-mode control in the process of speed synchronization in clutchless AMT systems, and enhanced the speed regulation control capability. Mohammadzadeh et al. [26] proposed a robust optimal speed synchronization control scheme. The control law consists of preview control, integral control, and state-feedback control, and an augmentation method is employed to minimize the effect of disturbance on the controlled output. In previous Refs. [27,28] the clutchless gear shift process has been described, and the identification of model parameters, coordinated control between EM and AMT, speed synchronization, and the actuator motion control are studied. However, most of the previous studies focused on the traditional synchronizer. Although the performance of the traditional synchronizer has been greatly improved, the inherent disadvantages of this synchronizer due to the limitations of the structure itself, including friction loss and excessive wear, have not been really solved.

Different from the research attentions of the available literature, this paper concentrates on a novel spring-based synchronizer which has a different internal structure from the traditional synchronizer, to overcome the drawbacks of the traditional synchronizer, decrease the energy consumption during gear change, improve the efficiency of transmission, and consequently extend the driving range of EVs. Unlike the traditional synchronizer that relies on friction torque to implement the speed synchronization process, the spring-based synchronizer uses a flexible part which is the torque spring to eliminate the speed difference between the target gear and the shaft. Since there are no friction elements involved in the speed synchronization process, the friction work and energy consumption in the synchronization stage, as well as wear of friction components will be greatly reduced. Furthermore, the temperature of the lubricating oil in the gearbox would not increase significantly during the shift process, which can greatly improve the performance and

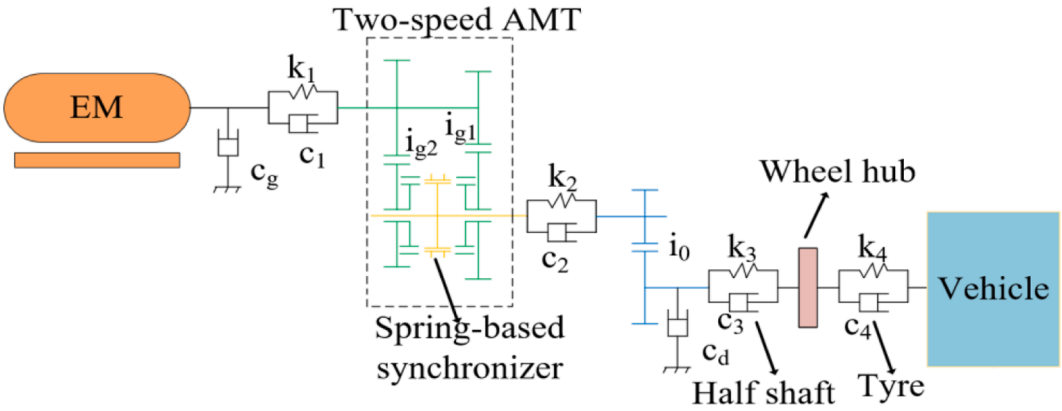

Fig. 2. Two-speed AMT powertrain model equipped with the new synchronizer.

efficiency of the gearbox. This paper will comprehensively compare the performance of traditional friction-based synchronizer and the novel spring-based synchronizer, including the engaging time, the power interruption time and the vehicle jerk. In addition, the influences of rotary inertia of EM, speed difference, spring stiffness and shift force on the engaging time and the vehicle jerk are quantitatively analyzed. Finally, several tactics of shift force control are proposed, such as single-closed loop proportional-integral (PI) position control, dual-closed loop PI control (an outed position loop and an inner velocity loop) and dual-closed loop fuzzy PI control, which further reduce the vehicle jerk.

The structure of this paper is shown as follows. Section 2 explains the working principle of the spring-based synchronizer. The vehicle dynamic model and the shift control model are built in Section 3, and the simulation results can show their different shift performance of the spring-based synchronizer and traditional synchronizer. The influences of rotary inertia of EM, speed difference, spring stiffness and shift force on the engaging time and the vehicle jerk are quantitatively analyzed in Section 4. Several control strategies of shift force are proposed in Section 5, which further reduce the vehicle jerk. The conclusions are drawn in the last section.

2. Principle analysis

2.1. Structure of the spring-based synchronizer

The spring-based synchronizer is mainly composed of sleeve, guide ring, dog gear, torque spring, hub, constant mesh gear and output shaft, shown as Fig. 1. The guide ring is located between the sleeve and the dog gear and fixed axially. Before synchronizing, it blocks the dog gear external grooves to prevent premature meshing. Four torque springs are installed in the internal groove of the dog gear, which flexibly connect the guide ring and the dog gear. As the torque springs are compressed or pulled due to the speed difference, torque will be transmitted through the springs to accelerate or decelerate the dog gear rapidly. The constant mesh gear is supported by a needle bearing and can rotate freely relative to the output shaft, but the axial position is fixed. The dog gear is fixed with the constant mesh gear so that they have the same angular speed. The chamfers of the guide ring teeth and the dog gear teeth can guide the sleeve teeth to insert their groove smoothly. In addition, there is a limiting mechanism between the guide ring and dog gear to avoid the full compression of the torque spring, which only allows the guide ring to rotate certain angular displacement relative to the dog gear.

Compared to the traditional synchronizer, the advantages of the proposed synchronizer are listed as follows:

(1) The novel synchronizer compresses or pulls the torque spring through the axial motion of the sleeve to open the guide ring and reaches the engaging position. By removing friction parts, the problem of friction-related, such as friction losses and wear, is overcome. Furthermore, the shifting shock can be absorbed by the springs to a certain extent during the meshing process.
(2) The spring-based synchronizer has fewer components than the traditional synchronizer, resulting in lower manufacturing cost, higher reliability and longer service life.
(3) Since the friction cone is removed from the proposed synchronizer, the influence of heat load due to friction loss is also greatly reduced so that the temperature of lubricant in the gearbox would not rise sharply during shift process, which can improve the transmission efficiency of EVs equipped with the AMT based on the proposed synchronizer.

It should be noted that the clutchless AMT equipped with the proposed spring-based synchronizer is only suitable for the circumstance that the speed difference between the sleeve and the dog gear is relatively small after the motor active speed regulation. If a gear shifting is performed under a large speed difference without speed regulation, large vehicle jerk may be generated when the sleeve directly engages the dog gear before the speed difference is completely eliminated by the torque provided by the compressed torque spring.

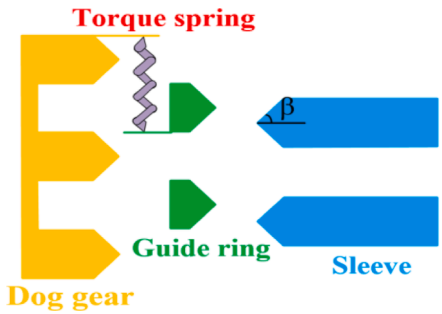

Fig. 3. Schematic diagram of the spring-based synchronizer.

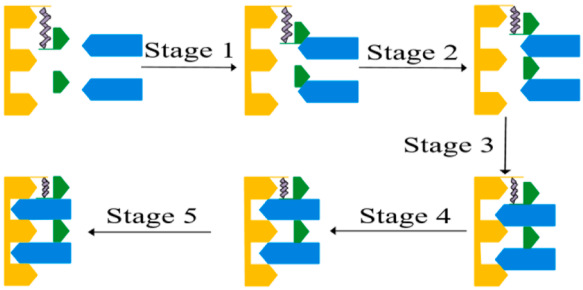

Fig. 4. The spring-based synchronizer engaging process.

2.2. Modeling of powertrain system

In this paper, an electric vehicle powertrain system based on the spring-based synchronizer is modeled as a multi-body model, as shown in Fig. 2. The EM is directly connected to the input shaft of the two-speed AMT. The output side of the driveline includes final gear, half shaft, wheel hubs, and vehicle equivalent inertia [29,30]. The dynamic equations of the model are as follows:

$$J_m\ddot{\theta}_m = T_m - k_1\left(\theta_m - \theta_g\right) - c_1\left(\dot{\theta}_m - \dot{\theta}_g\right) - c_g\dot{\theta}_m \tag{1}$$

$$J_d\ddot{\theta}_d = i_0\left[k_2(\theta_s - \theta_d i_0) + c_2\left(\dot{\theta}_s - \dot{\theta}_d i_0\right)\right] - k_3\left(\theta_d - \theta_w\right) - c_3\left(\dot{\theta}_d - \dot{\theta}_w\right) - c_d\dot{\theta}_d \tag{2}$$

$$J_w\ddot{\theta}_w = k_3(\theta_d - \theta_w) + c_3\left(\dot{\theta}_d - \dot{\theta}_w\right) - k_4\left(\theta_w - \theta_v\right) - c_4\left(\dot{\theta}_w - \dot{\theta}_v\right) \tag{3}$$

$$J_v\ddot{\theta}_v = k_4\left(\theta_w - \theta_v\right) + c_4\left(\dot{\theta}_w - \dot{\theta}_v\right) - T_f \tag{4}$$

where J_m is the EM inertia, J_d is the equivalent inertia reflected on the half shaft, J_w is the equivalent inertia of wheel hubs, J_v is the equivalent inertia of vehicle, including the tire inertia, θ denotes the angular displacement of each degree of freedom of the powertrain model, i_0 is the final ratio, c_j and k_j ($j = 1, 2, 3$) represent the damping and stiffness coefficients of each shaft, respectively, c_4 and k_4 are the tire damping coefficient and stiffness coefficient, c_g and c_d denote the vicious damping coefficient, T_m is the driving torque provided by the EM, T_f is the vehicle driving resistance moment.

2.3. Working process of the spring-based synchronizer

To clearly show the synchronization process, the spring-based synchronizer is simplified as shown in Fig. 3, and the entire working process is divided into five stages according to the axial position of sleeve as shown in Fig. 4.

Stage 1. The shift force pushes the sleeve to leave its neutral position and move toward the target gear. At this point, the guide ring and the dog gear rotate at the same speed and the torque spring is at the initial length. When the sleeve teeth contact with the guide ring, the engaging process enters the next stage. The motions can be described by the following formulas:

$$J_s^{'}\ddot{\theta}_s = -k_2(\theta_s - \theta_d i_0) - c_2\left(\dot{\theta}_s - \dot{\theta}_d i_0\right) \tag{5}$$

$$J_g^{'}\ddot{\theta}_g = k_1\left(\theta_m - \theta_g\right) + c_1\left(\dot{\theta}_m - \dot{\theta}_g\right) + \frac{1}{i_{gn}}\left[k_{sp}\left(\theta_{rn} - \theta_{gn}\right) + c_{sp}\left(\dot{\theta}_{rn} - \dot{\theta}_{gn}\right)\right] \tag{6}$$

$$J_{rn}\ddot{\theta}_{rn} = -k_{sp}\left(\theta_{rn} - \theta_{gn}\right) - c_{sp}\left(\dot{\theta}_{rn} - \dot{\theta}_{gn}\right) \tag{7}$$

$$m_s\ddot{x}_s = F_a - c_s\dot{x}_s - F_{r1} \tag{8}$$

where $J_s^{'}$ is an equivalent inertia including the sleeve and hub inertia, $J_g^{'}$ is the equivalent inertia on the input shaft, including the inertia of input shaft and all gear pairs of the transmission, J_{rn} is the guide ring inertia, m_s is the sleeve mass, x_s is the sleeve displacement and c_s is the viscous damping of the sleeve in axial motion, θ_m, θ_g, θ_{gn} ($n = 1, 2$), θ_s, θ_{rn} and θ_d represent the angular displacements of EM, input shaft, target gear, sleeve, guide ring and output shaft, respectively, i_{gn} represents the n-th gear ratio, k_{sp} and c_{sp} are the equivalent stiffness and damping coefficient of the torque spring, F_a is the axial shift force, F_{r1} is the axial resistance of the limiting device at the neutral position to the sleeve.

Stage 2. Due to the great resistance, the sleeve slides slowly along the guide ring teeth chamfers, and finally it is inserted into the guide hole to enter the next stage. At the same time, the sleeve teeth would squeeze the guide ring teeth chamfers, which results in the torque spring between the dog gear and the guide ring being compressed or pulled. Thus, the torque spring can provide a torque to gradually eliminate the speed difference between the sleeve and the dog gear. The motion equations regarding this phase are expressed as:

$$J_s^{'}\ddot{\theta}_s = -k_2(\theta_s - \theta_d i_0) - c_2\left(\dot{\theta}_s - \dot{\theta}_d i_0\right) + \left(F_a - c_s\dot{x}_s\right)R\frac{1 - \mu_s\tan\beta}{\tan\beta + \mu_s} \tag{9}$$

$$J_g^{'}\ddot{\theta}_g = k_1\left(\theta_m - \theta_g\right) + c_1\left(\dot{\theta}_m - \dot{\theta}_g\right) + \frac{1}{i_{gn}}\left[k_{sp}\left(\theta_{rn} - \theta_{gn}\right) + c_{sp}\left(\dot{\theta}_{rn} - \dot{\theta}_{gn}\right)\right] \tag{10}$$

$$J_{rn}\ddot{\theta}_{rn} = -k_{sp}\left(\theta_{rn} - \theta_{gn}\right) - c_{sp}\left(\dot{\theta}_{rn} - \dot{\theta}_{gn}\right) - \left(F_a - c_s\dot{x}_s\right)R\frac{1 - \mu_s\tan\beta}{\tan\beta + \mu_s} \tag{11}$$

$$m_s\ddot{x}_s = F_a - c_s\dot{x}_s - F_{r2} \tag{12}$$

where R is the mean contact radius between the sleeve and guide ring teeth, μ_s is chamfers friction coefficient of the guide ring teeth, β is the half angle of the sleeve, guide ring and dog gear teeth chamfers (as shown in Fig. 3), F_{r2} is the axial component of the normal force generated when the sleeve teeth contact with the guide ring teeth chamfers.

Stage 3. At the beginning of this stage, the sleeve teeth are in contact with the flat side of the guide ring. Under the action of shift force, the sleeve moves quickly again and passes through the guide hole, and the sleeve and the guide ring rotate at the same angular speed. This stage ends when the sleeve teeth are in contact with the chamfer of the dog gear teeth. The dynamic equations are shown as follows:

$$J_s^{'}\ddot{\theta}_s = -k_2(\theta_s - \theta_d i_0) - c_2\left(\dot{\theta}_s - \dot{\theta}_d i_0\right) - k_{sg}\left(\theta_s - \theta_{rn} - \frac{2\pi}{N}\right)^n - c_{sg}\left(\dot{\theta}_s - \dot{\theta}_{rn}\right) \tag{13}$$

$$J_g^{'}\ddot{\theta}_g = k_1\left(\theta_m - \theta_g\right) + c_1\left(\dot{\theta}_m - \dot{\theta}_g\right) + \frac{1}{i_{gn}}\left[k_{sp}\left(\theta_{rn} - \theta_{gn}\right) + c_{sp}\left(\dot{\theta}_{rn} - \dot{\theta}_{gn}\right)\right] \tag{14}$$

$$J_{rn}\ddot{\theta}_{rn} = -k_{sp}\left(\theta_{rn} - \theta_{gn}\right) - c_{sp}\left(\dot{\theta}_{rn} - \dot{\theta}_{gn}\right) + k_{sg}\left(\theta_s - \theta_{rn} - \frac{2\pi}{N}\right)^n + c_{sg}\left(\dot{\theta}_s - \dot{\theta}_{rn}\right) \tag{15}$$

$$m_s\ddot{x}_s = F_a - c_s\dot{x}_s - F_{r3} \tag{16}$$

where k_{sg} and c_{sg} are the equivalent stiffness and damping coefficient of collision between sleeve and guide ring, N ($N = 16$) is the number of sleeve teeth, n ($n = 2.2$) is nonlinear exponent factor, F_{r3} is the axial friction force generated by the side contact between the sleeve and the guide ring.

Stage 4. This stage starts when the sleeve teeth contact the dog gear teeth chamfers. Since the sleeve still contacts the flat flank of the guide ring, the rotational speeds of these two parts are identical. The sleeve slides slowly along the dog gear teeth chamfers until it is inserted into the dog gear teeth groove. Meanwhile, the sleeve teeth would squeeze the dog gear, which leads to the torque spring

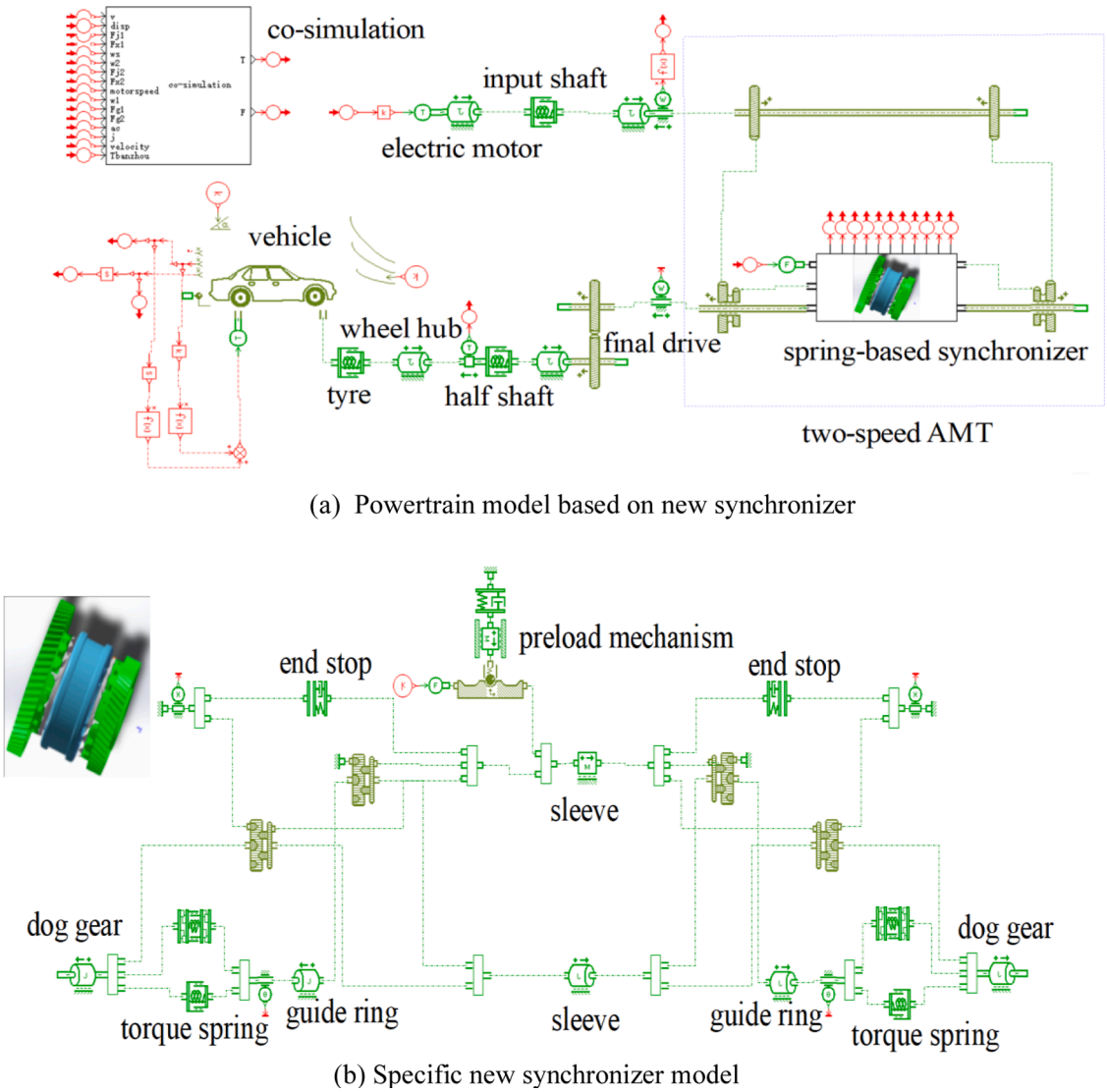

Fig. 5. Vehicle dynamics model based on new synchronizer. (a) Powertrain model based on new synchronizer. (b) Specific new synchronizer model.

further being compressed or pulled, providing a torque to reduce the speed difference and absorb the shifting shock. The equations of motion regarding this phase are the follows:

$$J_s'\ddot{\theta}_s = -k_2(\theta_s - \theta_d i_0) - c_2\left(\dot{\theta}_s - \dot{\theta}_d i_0\right) - k_{sg}\left(\theta_s - \theta_{rn} - \frac{2\pi}{N}\right)^n - c_{sg}\left(\dot{\theta}_s - \dot{\theta}_{rn}\right) + \left(F_a - c_s\dot{x}_s\right)R'\frac{1-\mu'_s\tan\beta}{\tan\beta + \mu'_s} \tag{17}$$

$$J_g'\ddot{\theta}_g = k_1\left(\theta_m - \theta_g\right) + c_1\left(\dot{\theta}_m - \dot{\theta}_g\right) + \frac{1}{i_{gn}}\left[k_{sp}\left(\theta_{rn} - \theta_{gn}\right) + c_{sp}\left(\dot{\theta}_{rn} - \dot{\theta}_{gn}\right)\right] - \frac{1}{i_{gn}}\left(F_a - c_s\dot{x}_s\right)R'\frac{1-\mu'_s\tan\beta}{\tan\beta + \mu'_s} \tag{18}$$

$$J_{rn}\ddot{\theta}_{rn} = -k_{sp}\left(\theta_{rn} - \theta_{gn}\right) - c_{sp}\left(\dot{\theta}_{rn} - \dot{\theta}_{gn}\right) + k_{sg}\left(\theta_s - \theta_{rn} - \frac{2\pi}{N}\right)^n + c_{sg}\left(\dot{\theta}_s - \dot{\theta}_{rn}\right) \tag{19}$$

$$m_s\ddot{x}_s = F_a - c_s\dot{x}_s - F_{r4} \tag{20}$$

where R' is the mean contact radius between the sleeve and dog gear teeth, μ_s' is chamfers friction coefficient of the dog gear teeth, F_{r4} is the axial component of the normal force generated when the sleeve teeth contact with the dog gear teeth chamfers.

Stage 5. During the stage, the sleeve teeth quickly pass through the dog gear teeth groove and reach the bottom. The sleeve, guide ring and dog gear rotate at the same speed, indicating that the engaging process completes. The motion equations can be written as

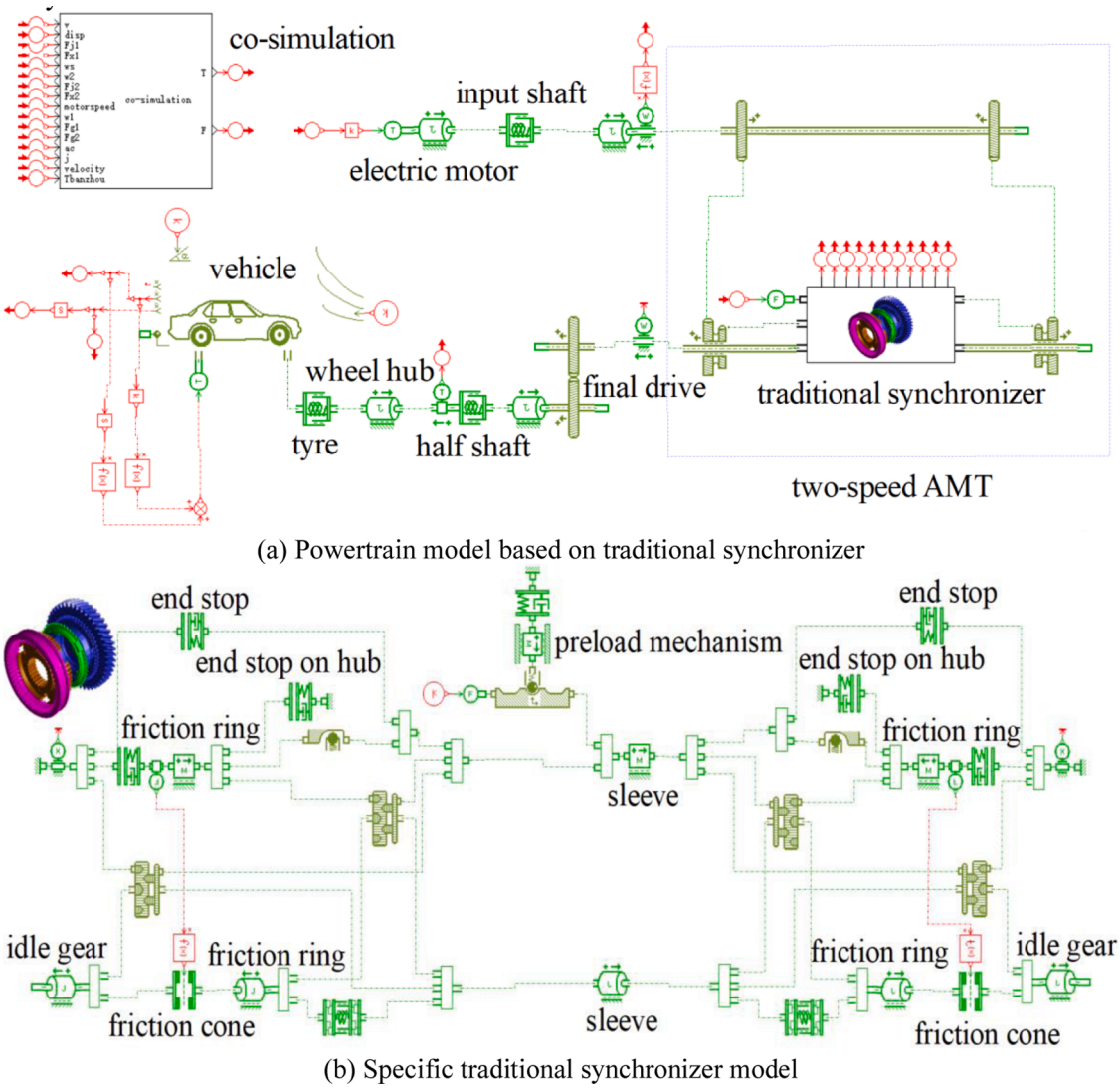

Fig. 6. Vehicle dynamics model based on traditional synchronizer. (a) Powertrain model based on traditional synchronizer. (b) Specific traditional synchronizer model.

follows:

$$J_g'\ddot{\theta}_g = k_1(\theta_m - \theta_g) + c_1\left(\dot{\theta}_m - \dot{\theta}_g\right) + \frac{1}{i_{gn}}\left[k_{sp}(\theta_{rn} - \theta_{gn}) + c_{sp}\left(\dot{\theta}_{rn} - \dot{\theta}_{gn}\right)\right] + \frac{1}{i_{gn}}\left[k_{sd}\left(\theta_s - \theta_{gn} - \frac{2\pi}{N}\right)^n + c_{sd}\left(\dot{\theta}_s - \dot{\theta}_{gn}\right)\right] \tag{21}$$

$$J_g'\ddot{\theta}_g = k_1(\theta_m - \theta_g) + c_1\left(\dot{\theta}_m - \dot{\theta}_g\right) + \frac{1}{i_{gn}}\left[k_{sp}(\theta_{rn} - \theta_{gn}) + c_{sp}\left(\dot{\theta}_{rn} - \dot{\theta}_{gn}\right)\right] + \frac{1}{i_{gn}}\left[k_{sd}\left(\theta_s - \theta_{gn} - \frac{2\pi}{N}\right)^n + c_{sd}\left(\dot{\theta}_s - \dot{\theta}_{gn}\right)\right] \tag{22}$$

$$J_{rn}\ddot{\theta}_{rn} = -k_{sp}(\theta_{rn} - \theta_{gn}) - c_{sp}\left(\dot{\theta}_{rn} - \dot{\theta}_{gn}\right) + k_{sg}\left(\theta_s - \theta_{rn} - \frac{2\pi}{N}\right)^n + c_{sg}\left(\dot{\theta}_s - \dot{\theta}_{rn}\right) \tag{23}$$

$$m_s\ddot{x}_s = F_a - c_s\dot{x}_s - F_{r5} \tag{24}$$

where k_{sd} and c_{sd} are the equivalent stiffness and damping coefficient of collision between the sleeve and the dog gear, F_{r5} is the axial friction force generated by the side contact between the sleeve and the dog gear.

At the end of the shift process, the sleeve teeth were fully inserted into the dog gear groove. Meanwhile, the sleeve, guide ring and dog gear rotate at the same speed. The dynamic equations are expressed as:

Table 1
Partial parameters of synchronizer dynamics models.

Parameters	Traditional synchronizer	Novel synchronizer
Number of teeth	16	
Axial clearance between the sleeve teeth top and the ring teeth top	0.312 mm	2.8 mm
Axial clearance between the sleeve teeth top and the gear teeth top	6.61 mm	
Sleeve/ring/gear teeth half width	3 mm	
Maximum axial displacement of the sleeve	12.11 mm	
Mass of the sleeve	0.8 kg	
Viscous friction coefficient of sleeve	85 N/(m/s)	
The half angle of the sleeve, ring and gear teeth chamfers	60°	

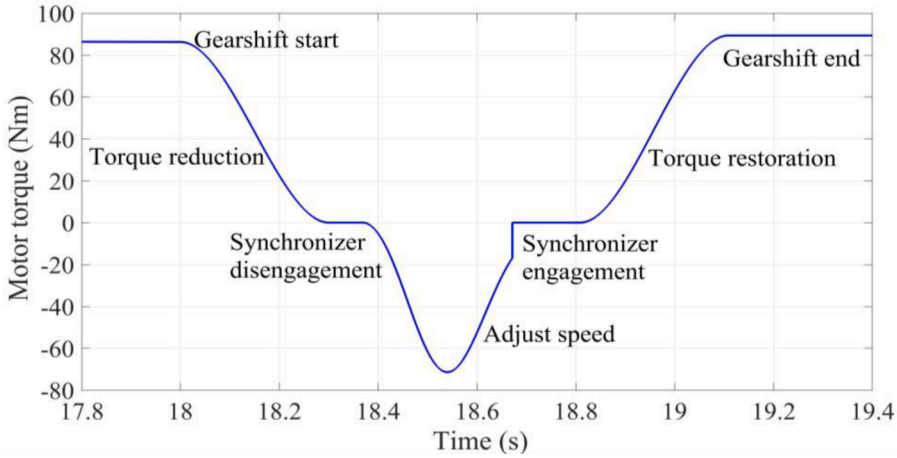

Fig. 7. Shift control of motor torque.

$$\left(J_s' + J_m + J_g' i_{gn}^2\right)\ddot{\theta}_s = \left[k_1\left(\theta_m - \theta_g\right) + c_1\left(\dot{\theta}_m - \dot{\theta}_g\right)\right] i_{gn} - k_2(\theta_s - \theta_d i_0) - c_2\left(\dot{\theta}_s - \dot{\theta}_d i_0\right) \tag{25}$$

$$m_s \ddot{x}_s = 0 \tag{26}$$

It should be noted that after the completion of the shift, the torque spring will always be compressed. When the next shift begins, the sleeve will move axially from the engaging position back to the neutral position. At the same time, the guide ring will rotate back to its original position under the rotating force of the torque spring compression or stretching.

3. Modeling and simulating

3.1. Vehicle dynamics modeling in AMESim environment

In this paper, based on the above detailed introduction of the shift process as well as the dynamics equation, the two-speed clutchless AMT vehicle dynamics model based on the new synchronizer is established using the AMESim software, shown as Fig. 5. Meanwhile, the vehicle dynamics model based on the traditional synchronizer is established for quantitative comparison, shown as Fig. 6.

The difference between the two models lies in the synchronizer module. For the traditional synchronizer, the friction ring can move axially, and the elimination of the speed difference depends on the friction torque generated by the interaction between the friction cone of the friction ring and the idle gear. But with the spring-based synchronizer, the guide ring is axially fixed, and the speed difference is removed by the torque produced by the compression or stretching of the torque spring mounted in the internal grooves of the dog gear. Some important parameters of the specific synchronizer dynamics model are shown in Table 1.

3.2. Shift control modeling in MATLAB/Simulink environment

The change of motor torque during shift process is shown in the Fig. 7, and the shift control process for the clutchless AMT mainly includes five steps as follows:

Step 1. Motor torque reduction. When the gear shift begins, the motor torque gradually decreases to zero.

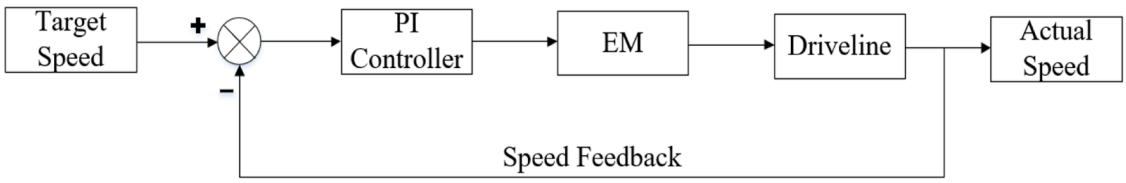

Fig. 8. PI controller for adjusting dog gear speed.

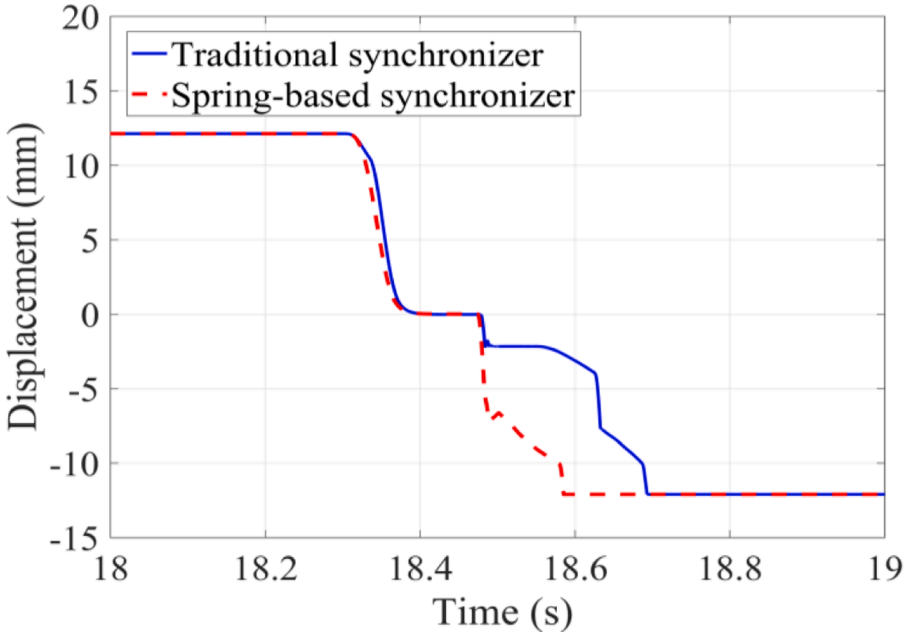

Fig. 9. Sleeve displacement of traditional synchronizer and spring-based synchronizer.

Step 2. Synchronizer disengagement. When the motor torque is set to zero, the sleeve would move axially from the engaging position back to the neutral position under the shift force.

Step 3. Motor speed control. When the sleeve reaches the neutral position, the EM actively adjusts the target gear speed by PI control (shown as Fig. 8) until the speed difference between the sleeve and the dog gear reaches a threshold value that allows the sleeve to engage with a small speed difference.

Step 4. Synchronizer engagement. When the speed difference reaches the threshold value and the motor torque becomes zero, the sleeve will move axially from the neutral position to the next engaging position under the shift force. At this stage, the residual speed difference is eliminated by the torque provided by the compression or tension of torque spring which flexibly connects the dog gear and the guide ring, or friction torque generated by the interaction between the friction cone of the friction ring and the idle gear.

Step 5. Motor torque restoration. When the sleeve reaches the engaging position, the EM torque gradually increases to the demand level.

Based on the above analysis, a two-gear AMT vehicle shift control model is established in Matlab/Simulink software. Then, AMESim and Simulink are used to carry out the co-simulation, and the simulation results are compared and analyzed.

3.3. Comparison of simulation results

In order to quantitatively evaluate the gear shift quality of two kinds synchronizers, three evaluation indexes are proposed, which are the engaging time (t_s), the power interruption time (t_p) and the vehicle jerk (j_v). The engaging time refers to the time required for the sleeve to move axially from the neutral position to the engaging position. The power interruption time refers to the time when the vehicle acceleration is less than zero during the whole shift process. The vehicle jerk is defined as the change rate of vehicle longitudinal acceleration as follows:

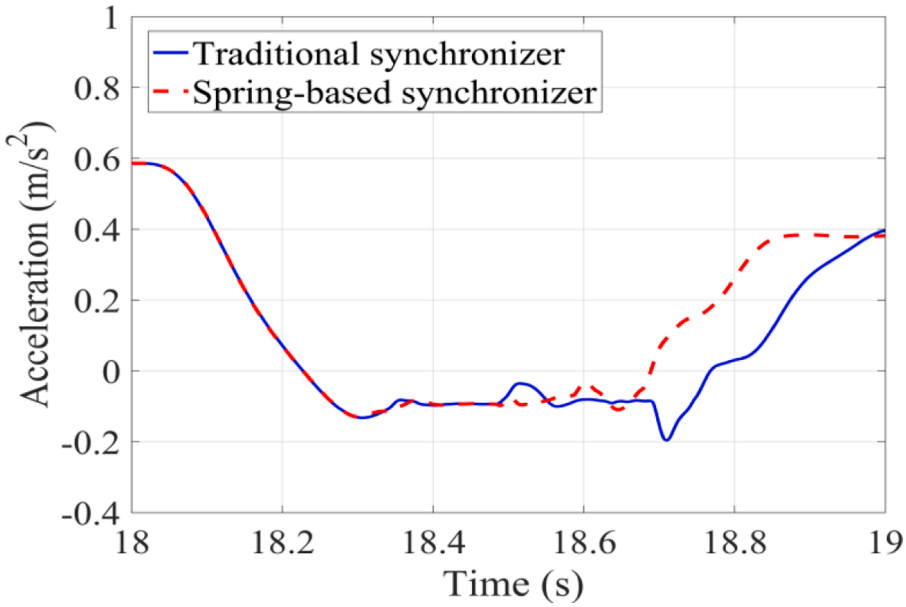

Fig. 10. Vehicle acceleration of traditional synchronizer and spring-based synchronizer.

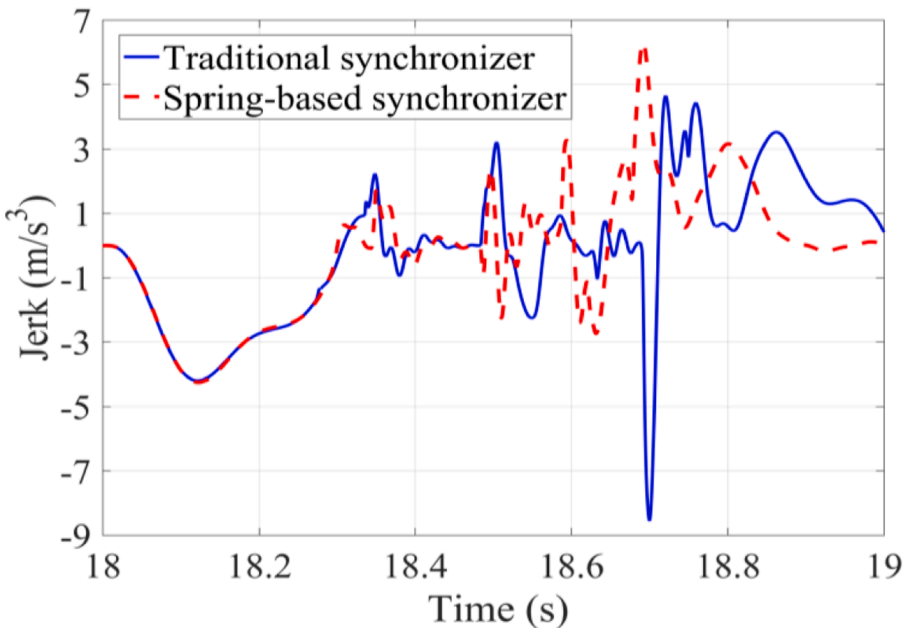

Fig. 11. Vehicle jerk of traditional synchronizer and spring-based synchronizer.

Table 2
Shift quality of two types of synchronizers.

	t_s (s)	t_p (s)	$\lvert j_v \rvert_{max}$ (m/s^3)
Traditional synchronizer	0.2150	0.5412	8.5561
Spring-based synchronizer	0.1112	0.4616	6.2900
Percentage improvement	48.3%	19.3%	26.5%

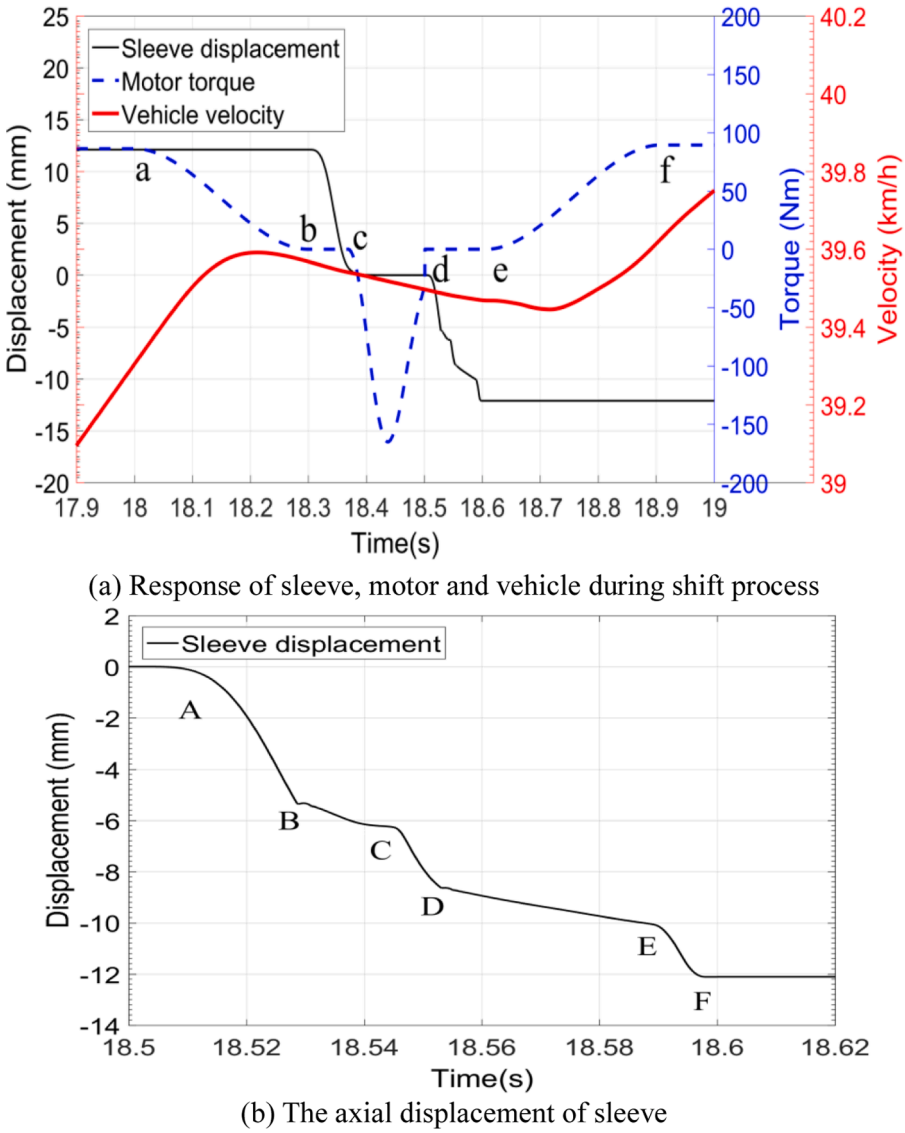

Fig. 12. Whole shift process of spring-based synchronizer. (a) Response of sleeve, motor and vehicle during shift process. (b) The axial displacement of sleeve.

$$j_v = \frac{d^2 v}{dt^2} \tag{27}$$

where v is the vehicle longitudinal velocity, and t is the time. With the decrease of t_s, t_p and j_v, the shift quality becomes better.

In order to compare the two kinds synchronizers fairly, model parameters, for example, the rotary inertia of EM, the tooth shape and the vehicle mass, are set to the same. Then, the simulation is carried out under the identical gear shift conditions, such as the same speed difference (30 rpm) and shift force (150 N). The simulation results are shown in Figs. 9–11. It can be found from Fig. 9 that the proposed synchronizer can considerably reduce the engaging time than the traditional one. The torque spring of the novel synchronizer can provide a torque to reduce the speed difference during engagement. This helps to reduce the shifting shock significantly. Therefore, the maximum vehicle jerk decreases from about 8.5561 m/s^3 to 6.2900 m/s^3 (Fig. 11). Table 2 shows the comparison of the shifting quality of the traditional synchronizer and the proposed spring-based synchronizer.

According to the above table, the spring-based synchronizer has a great improvement in terms of the engaging time (t_s), the power interruption time (t_p) and the vehicle jerk (j_v), compared with the traditional synchronizer. Hence, the two-speed AMT with the spring-based synchronizer can achieve higher shift quality.

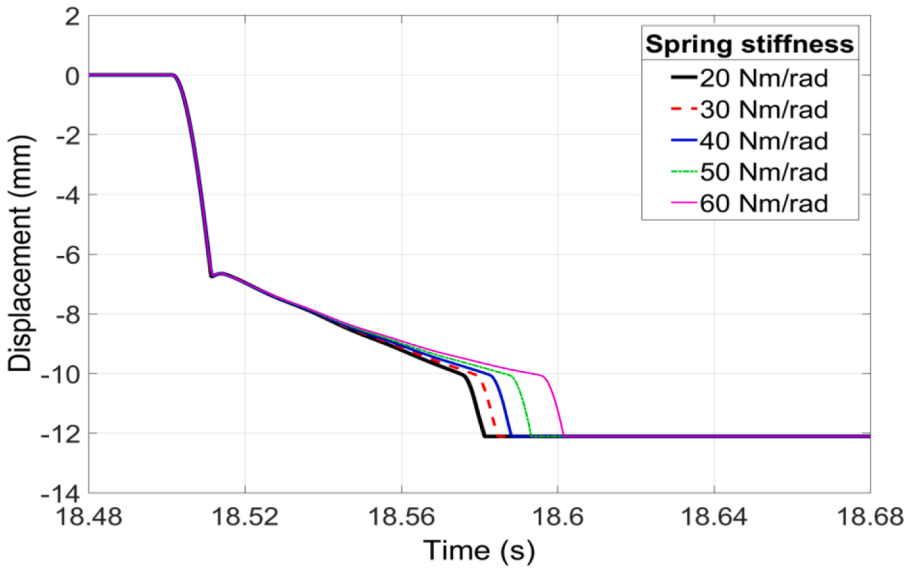

Fig. 13. Displacement under different spring stiffness.

3.4. Analysis of simulation results

In this section, the whole shift process based on the novel synchronizer described above is verified according to the simulation results. As shown in Fig. 12(a), the shift process can be divided into five steps.

Step 1 ($t_a - t_b$): The shift process starts at t_a, then the motor torque begins to drop until it reaches zero at t_b. During this process, the vehicle velocity begins to decrease and the sleeve is still in 1nd gear.

Step 2 ($t_b - t_c$): The sleeve starts to leave the engagement position and reaches the neutral position at t_c. In this stage, the motor torque remains zero and the vehicle velocity continues to decrease.

Step 3 ($t_c - t_d$): After the sleeve reaches the neutral position, the motor starts to actively adjust the speed of the target gear until it reaches the target speed at t_d. At this phase, the position of the sleeve remains unchanged and the vehicle velocity continues to decrease.

Step 4 ($t_d - t_e$): When the speed difference between the shaft and the target gear reaches the threshold value, the sleeve starts to leave the neutral position and reaches the engagement position at t_e. In this stage, the motor torque remains zero and the vehicle velocity continues to decrease.

Step 5 ($t_e - t_f$): After the sleeve reaches the engagement position, the motor torque begins to increase and reaches the target torque at t_f, indicating the end of the whole shift process. During this process, the vehicle velocity begins to increase and the sleeve is still in 2nd gear.

Furthermore, the Step 4 (synchronizer's engagement) can be divided into five more detailed stages (see Fig. 12(b)).

Stage 1 ($t_A - t_B$): When at t_A, the sleeve is at the neutral position. Under the shift force, the sleeve begins to move quickly and approaches the guide ring, and it contacts the guide ring at t_B, resulting in a significant decrease in its velocity.

Stage 2 ($t_B - t_C$): The sleeve slides slowly along the guide ring teeth chamfers, and finally it is inserted into the guide hole at t_C. At this stage, the torque spring will be compressed or pulled to produce a torque.

Stage 3 ($t_C - t_D$): The sleeve passes through the guide hole quickly. Then, the sleeve contacts the dog gear at t_D, leading to a significant decrease in its velocity.

Stage 4 ($t_D - t_E$): The sleeve slides slowly along the dog gear teeth chamfers. Then at t_E, the sleeve is inserted into the dog gear teeth groove.

Stage 5 ($t_E - t_F$): The sleeve passes rapidly through the dog gear teeth groove and finally reaches the bottom at t_F. In conclusion, the effectiveness of the dynamics model and the shift control model is validated through the simulation results.

4. Influences of some parameters on shift performance

Based on the model built in Section 3, this section focuses on the influence of spring stiffness, speed difference, rotary inertia of EM and shift force on the engaging time and the vehicle jerk by using the control variable method, respectively. In order to quantify the impact of these factors on the vehicle jerk, the torque restoration is abandoned in the simulation. The motor torque remains zero after engagement, because torque restoration also generates jerk.

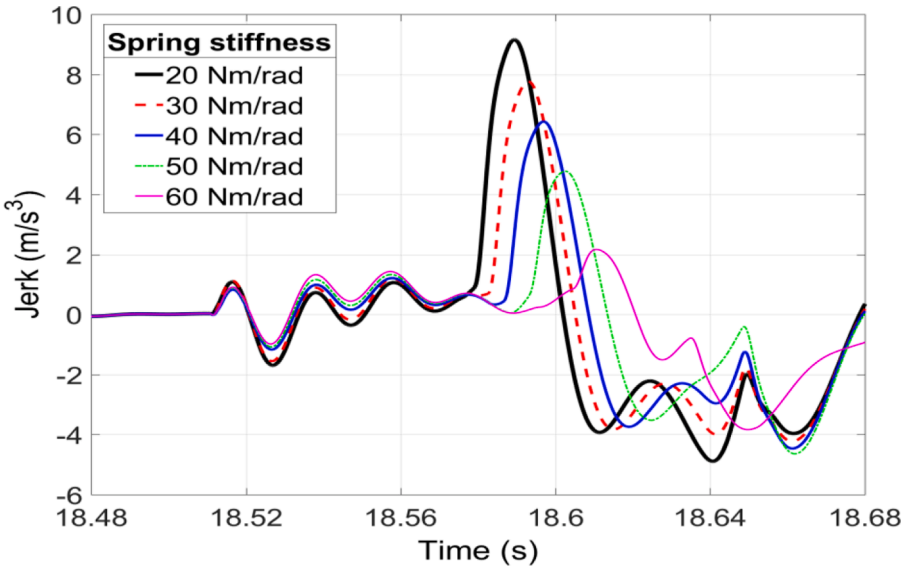

Fig. 14. Jerk under different stiffness.

Table 3
Shift quality under different spring stiffness.

Spring stiffness (Nm/rad)	20	30	40	50	60
t_s (s)	0.0802	0.0836	0.0872	0.0922	0.1006
$\lvert j_v \rvert_{max}$ (m/s^3)	9.1547	7.7705	6.4312	4.7732	3.8373

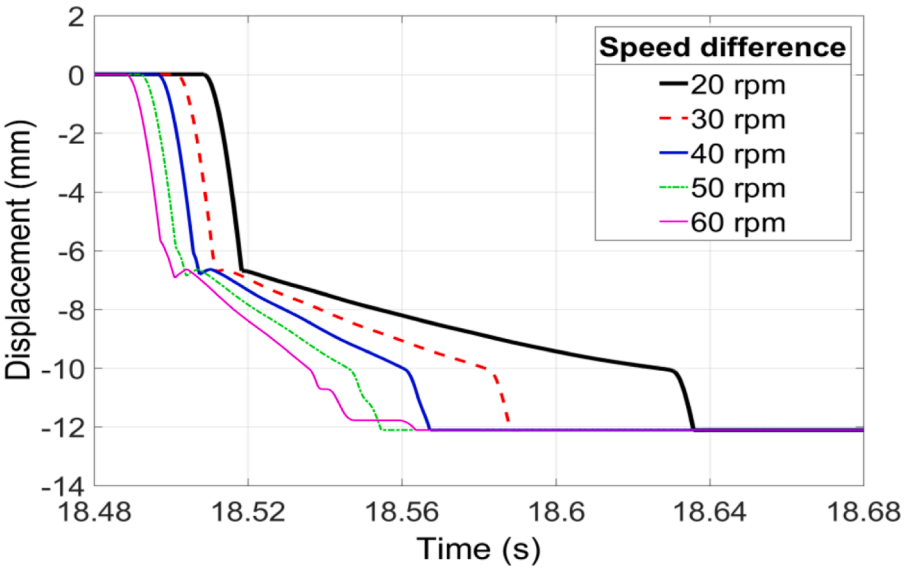

Fig. 15. Displacement under different speed differences.

4.1. Influence of spring stiffness

During engagement, the torque springs of the spring-based synchronizer play a vital role in eliminating residual speed difference, absorbing the torsional vibrations and reducing the vehicle jerk. Hence, it is necessary to study the influence of spring stiffness on shift quality. On the premise of the same other parameters, the torque springs with different stiffness are selected for simulation, as shown in Figs. 13 and 14. Then the engaging time (t_s) and the vehicle jerk (j_v) under different spring stiffness are listed in Table 3.

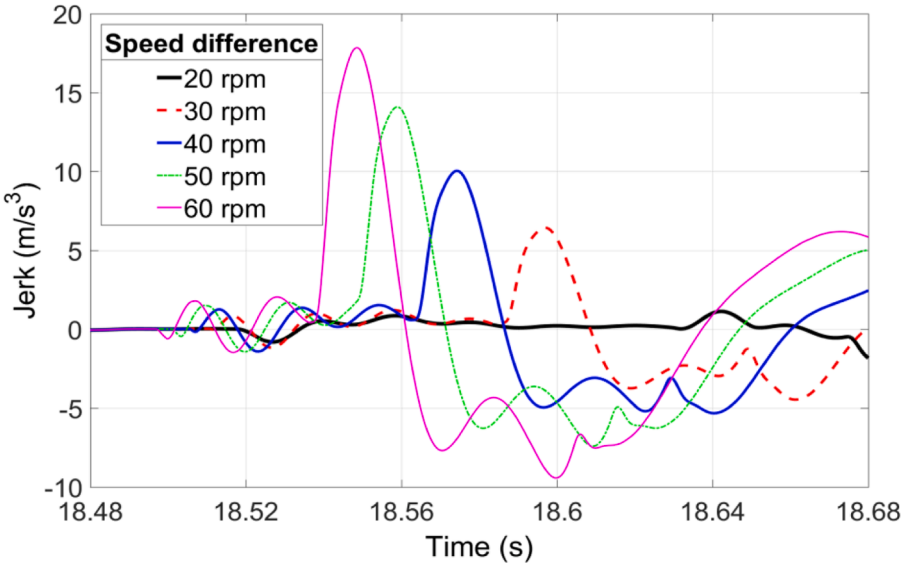

Fig. 16. Jerk under different speed differences.

Table 4
Shift quality under different speed difference.

Speed difference (rpm)	20	30	40	50	60
t_s (s)	0.1278	0.0872	0.0710	0.0628	0.0750
$\lvert j_v \rvert_{max}$ (m/s^3)	2.6927	6.4312	10.0398	14.0868	17.8458

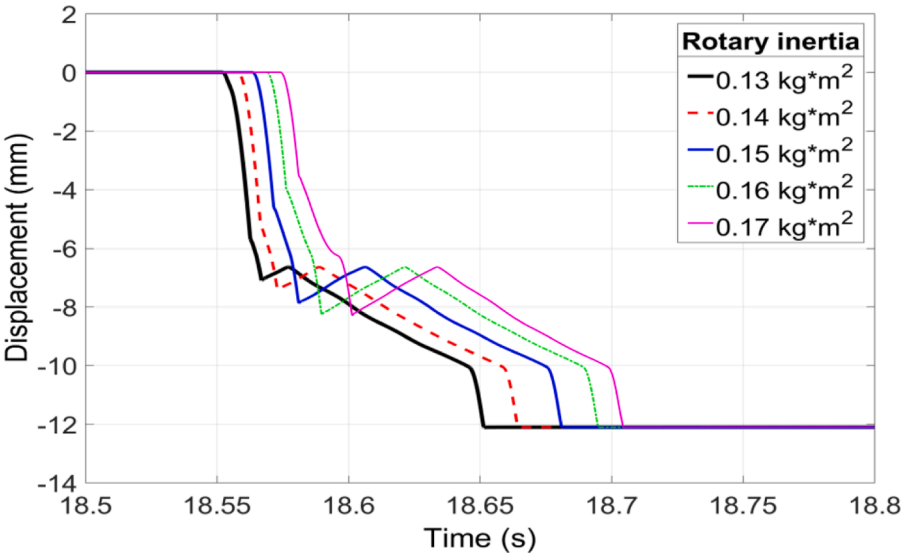

Fig. 17. Displacement under different rotary inertia.

It can be seen from Table 3 that, with the increase of spring stiffness, the engaging time is gradually increasing, whereas the vehicle jerk is gradually decreasing. The increase of the spring stiffness can better absorb the impact energy caused by the different speed of the sleeve and the dog gear, which can reduce the vehicle jerk. But the increase of spring stiffness also increases the resistance of the sleeve when it moves axially, which would lead to the prolongation of the engaging time. Therefore, an appropriate spring stiffness should be selected to ensure that the engaging time and the vehicle jerk can be controlled within a reasonable range.

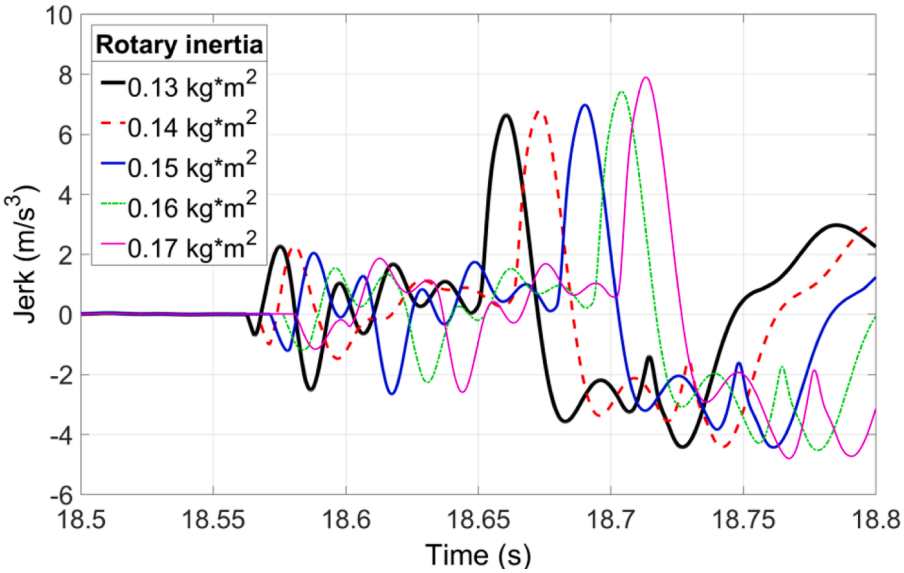

Fig. 18. Jerk under different rotary inertia.

Table 5
Shift quality under different rotary inertia.

Rotary inertia (kg*m^2)	0.13	0.14	0.15	0.16	0.17
t_s (s)	0.0966	0.1066	0.1178	0.1262	0.1304
$\lvert j_v \rvert_{max}$ (m/s^3)	6.6383	6.7996	6.9772	7.4225	7.8970

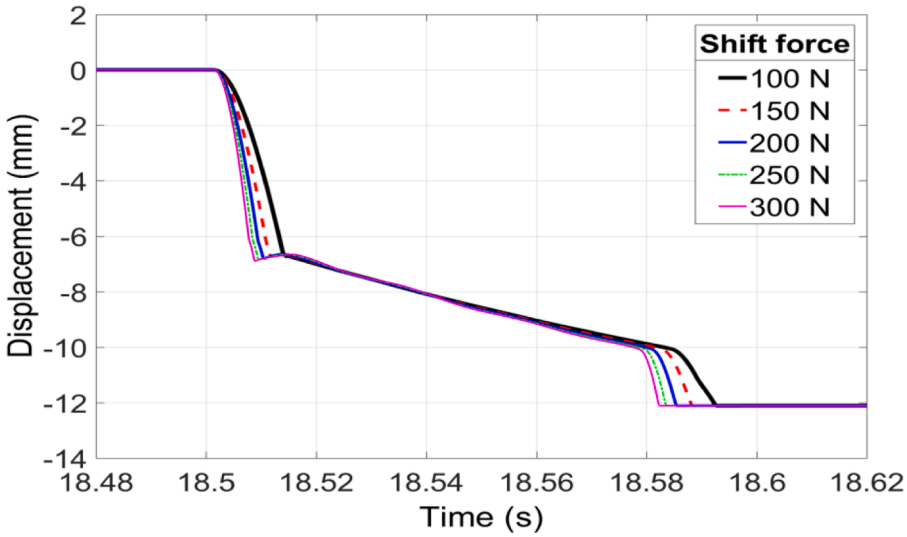

Fig. 19. Displacement under different shift force.

4.2. Influence of speed difference

The speed difference between the shaft and the target gear also has a great effect on shift quality. Figs. 15 and 16 show the displacement of sleeve and the vehicle jerk under different speed differences. Then the engaging time (t_s) and the vehicle jerk (j_v) under different speed differences are listed in Table 4.

As can be seen from Table 4, with the increase of the speed difference, the engaging time decreases, while the vehicle jerk gradually increases. However, when the speed difference is too large, not only the vehicle jerk but also the engaging time would increase. This

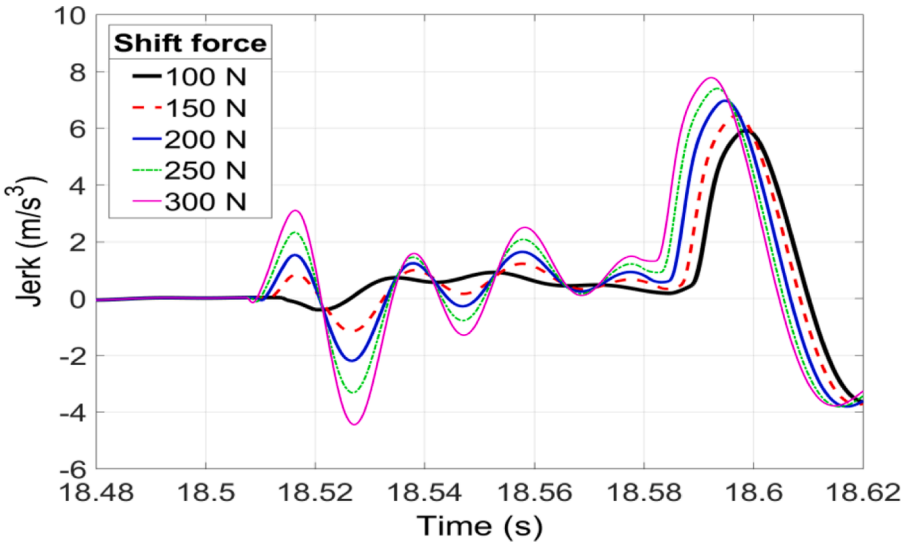

Fig. 20. Jerk under different shift force.

Table 6
Shift quality under different shift force.

Shift force (N)	100	150	200	250	300
t_s (s)	0.0914	0.0872	0.0844	0.0821	0.0812
$\lvert j_v \rvert_{max}$ (m/s^3)	5.9122	6.4312	6.9596	7.3917	7.7760

means that in order to improve the shifting quality for the spring-based synchronizer, the speed difference should be in a reasonable range. The increase of the speed difference is beneficial for the sleeve teeth to slide into the guide ring hole or dog gear slot, but it would cause greater shift shock, which would lead to higher vehicle jerk. The sleeve would have a small range of reverse movement in the collision stage with the guide ring or dog gear under the great speed difference, resulting in the increase of the engaging time.

4.3. Influence of rotary inertia

This study focuses on the influence of rotary inertia on the shift quality. The displacement of sleeve and the vehicle jerk under different rotary inertia are shown in Figs. 17 and 18, respectively. Then the engaging time (t_s) and the vehicle jerk (j_v) are listed in Table 5.

It can be seen from Table 5 that with the increase of rotary inertia, both engaging time and vehicle jerk would increase. The increase of rotary inertia would increase the speed synchronization time and the shift shock, which leads to the prolongation of the engaging time and the increase of the vehicle jerk.

4.4. Influence of shift force

The impact of shift force on the shift quality is investigated in this section. The displacement of sleeve and the vehicle jerk under different shift force are presented in Fig. 19 and Fig. 20, respectively. Then the engaging time (t_s) and the vehicle jerk (j_v) are listed in Table 6.

As can be seen from the above table, with the increase of the shift force, the engaging time is gradually decreasing and the vehicle jerk is gradually increasing. The larger shift force could accelerate the axial velocity of the sleeve, making the sleeve reach the meshing position faster, and reducing the engaging time. However, the high axial velocity of the sleeve would cause a large shock at the time of contact, which would increase the vehicle jerk.

5. Shift force control

The above simulation results are based on the constant shift force to push the sleeve. In order to further improve the shift quality, several shift force control methods, which are PI position control, dual-closed loop PI control (an outed position loop and an inner velocity loop) and dual-closed loop fuzzy PI control, are proposed. Then the simulation results are compared under the premise of the same model parameters and shift conditions, for example, the spring stiffness is 50 Nm/rad, the speed difference is 30 rpm.

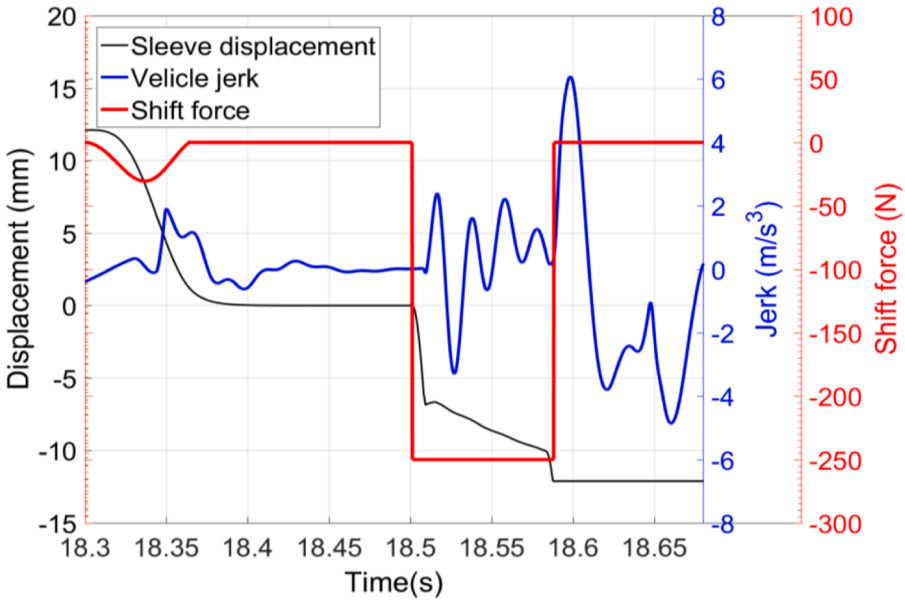

Fig. 21. Shift performance of constant shift force.

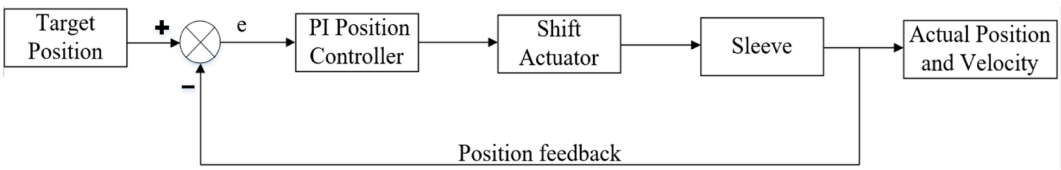

Fig. 22. Schematic diagram of PI position controller.

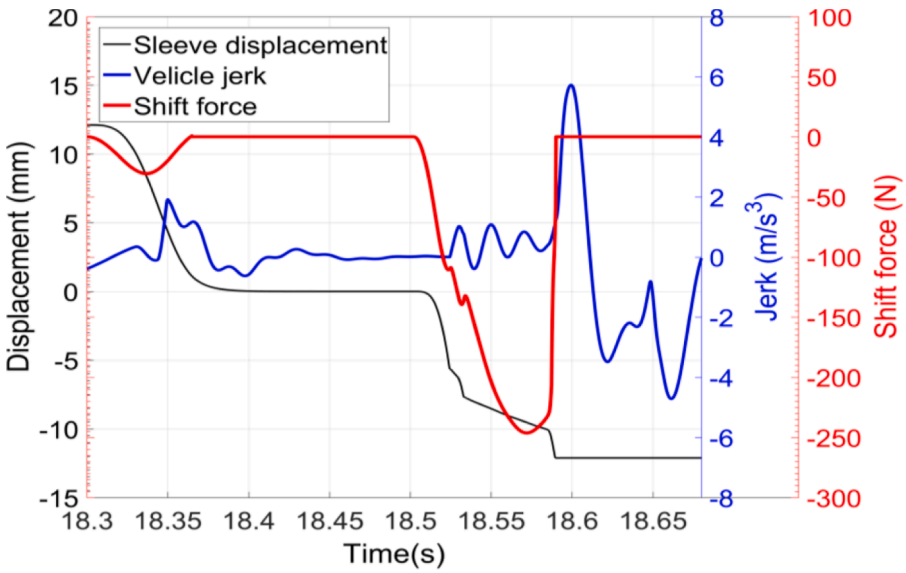

Fig. 23. Shift performance of PI position controller.

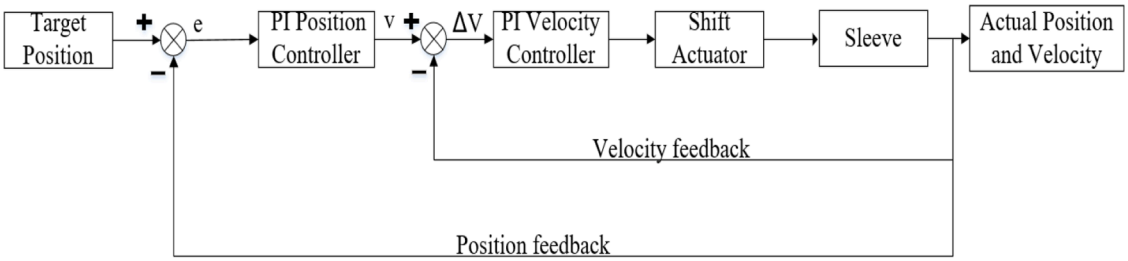

Fig. 24. Schematic diagram of the dual-closed loop PI controller.

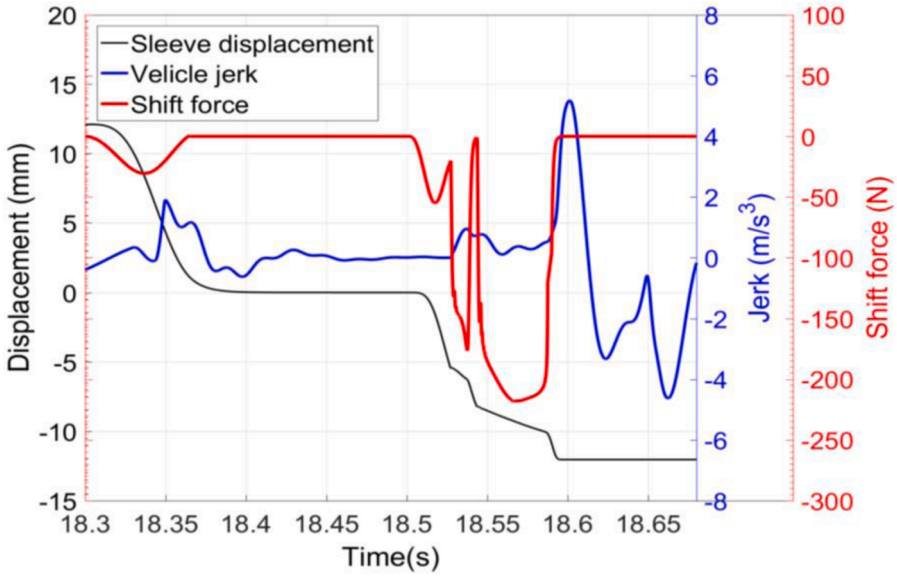

Fig. 25. Shift performance of dual-closed loop PI controller.

5.1. Constant shift force

Constant shift force is an open-loop control. Although the structure of the open-loop control is simple, it cannot adapt to the whole shift process well due to the nonlinear engagement process. Constant shift force may make the axial velocity of the sleeve greater before the collision, resulting in greater shift shock. The simulation results are shown in the Fig. 21. From the figure, it can be found that the maximum vehicle jerk is 6.1054 m/s^3.

5.2. PI position control

PI control is a general control method, which is widely used in many industrial control systems due to its functional simplicity and reliability performance. The equation fora typical PI controller is given by Eq. (28).

$$u(t) = K_p e(t) + K_i \int e(t)dt \tag{28}$$

where u is the output signal from PI controller, e is the error signal, t is the time, K_p and K_i are proportional and integral gains, respectively.

In this study, the difference between the target position and the actual position of the sleeve is the input of the PI controller, so as to change the shift force in real time. Fig. 22 shows the schematic diagram of controlling the shift force through PI position controller.

PI position controller is used in the model, and the simulation results are shown in the Fig. 23. As shown in Fig. 23, compared to the open loop control above, which uses a constant shift force to push the sleeve, the PI control adjusts the shift force in real time according to the actual displacement of the sleeve. This can reduce the velocity of the sleeve before it collides with the guide ring, the dog gear, or the limiting device. Consequently, the maximum vehicle jerk reduces from 6.0816 m/s^3 (Fig. 21) to 5.7207 m/s^3 (Fig. 23).

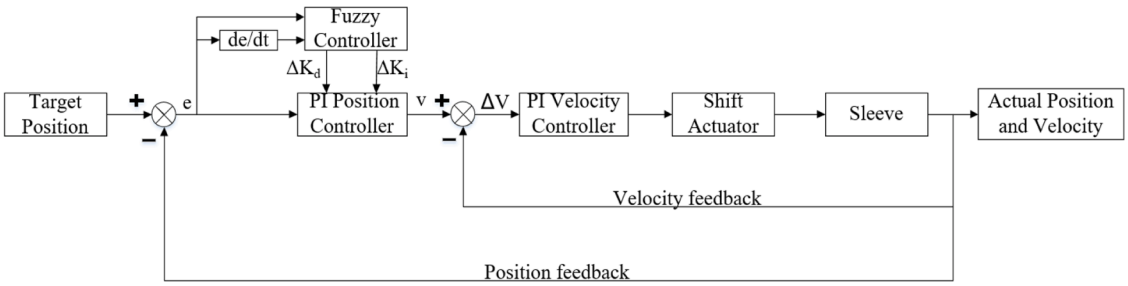

Fig. 26. Schematic diagram of the dual-closed loop fuzzy PI controller.

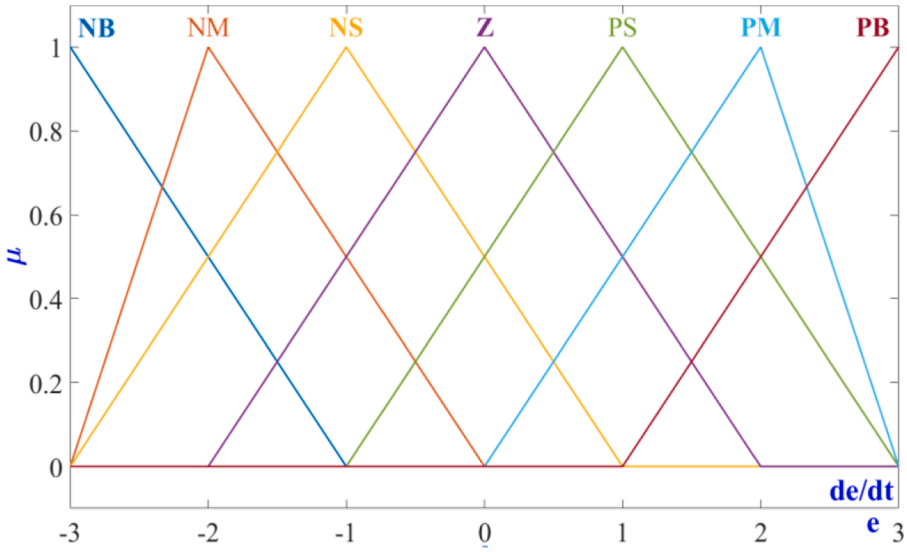

Fig. 27. Membership function for fuzzy inputs.

5.3. Dual-closed loop PI control

In order to further control the velocity of the sleeve before collision and reduce the shift shock, a dual-closed loop PI controller (an outer position loop and an inner velocity loop) is used in the model. For the outer position loop, the input is the position deviation (e) between the target position and the current position of the sleeve, and the output is the target control velocity of the sleeve. For the inner velocity loop, the input is the velocity deviation Δv between the target velocity and the actual velocity of the sleeve, and the output is transformed into shift force to push the sleeve to move axially through the shift actuator. Fig. 24 displays the schematic diagram of the dual-closed loop PI controller.

The dual-closed loop PI controller is used in the model, and the simulation results are shown in the Fig. 25. Compared with the above PI controller which only controls the shift force according to the real-time displacement of the sleeve, the double closed-loop PI controller can also control the shift force according to the real-time velocity of the sleeve. As the velocity of the sleeve approaches the allowable value, the shift force is reduced, which further reduces the velocity before the sleeve collides with the guide ring, the dog gear, or the limiting device. Consequently, the maximum vehicle jerk reduces to 5.1814 m/s^3.

5.4. Dual-closed loop fuzzy PI control

Fuzzy control has strong anti-disturbance and self-adaptive ability. Since the parameters in the traditional PI controller cannot be changed once they are set, fuzzy control rules are introduced into the dual-closed loop PI controller, so as to further reduce the shift shock and improve the control accuracy of the electric shift actuator.

The fuzzy PI controller includes fuzzy controller and PI controller. The fuzzy controller takes the position deviation (e) and the deviation change rate (de/dt) of the sleeve as the input, and through fuzzy reasoning, the output is the variation of K_p and K_i (ΔK_p and ΔK_i) in PI controller. The fuzzy PI controller detects the e and the de/dt in real time during the control process, and adjusts the values of K_p and K_i in real time, as follows:

$$K_p = K_{p0} + \Delta K_p \tag{28}$$

Table 7
Fuzzy control rule table of ΔK_p.

e	de/dt						
	NB	NM	NS	Z	PS	PM	PB
NB	Z	Z	NM	NM	NM	NB	NB
NM	PS	Z	NS	NM	NM	NM	NB
NS	PS	PS	Z	NS	NS	NM	NM
Z	PM	PM	PS	Z	NS	NM	NM
PS	PM	PM	PM	PS	Z	NS	NS
PM	PB	PB	PM	PS	PS	Z	NS
PB	PB	PB	PM	PM	PS	Z	Z

Table 8
Fuzzy control rule table of ΔK_i.

e	de/dt						
	NB	NM	NS	Z	PS	PM	PB
NB	NB	NB	NM	NM	NS	Z	Z
NM	NB	NB	NM	NS	NS	Z	Z
NS	NB	NM	NS	NS	Z	PS	PS
Z	NM	NM	NS	Z	PS	PM	PM
PS	NM	NS	Z	PS	PS	PM	PB
PM	Z	Z	PS	PS	PM	PB	PB
PB	Z	Z	PS	PM	PM	PB	PB

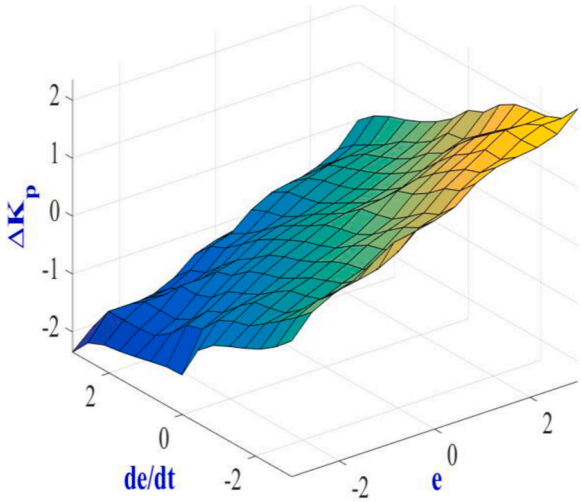

Fig. 28. The change in ΔK_p with e and de/dt.

$$K_i = K_{i0} + \Delta K_i \tag{29}$$

where K_{p0} and K_{i0} are the initial values of proportional and integral gains, respectively. Fig. 26 is the schematic diagram of the dual-closed loop fuzzy PI controller.

The language variables of input and output are defined as follows: e, de/dt, ΔK_p, ΔK_i. For the convenience of calculation, the above variable domains are defined as {- 3, - 2, - 1, 0, 1, 2, 3}, where e and de/dt are quantized to the domains by their quantization factors, respectively, while ΔK_p and ΔK_i are input to PI controller after their scale factor transformation, respectively. Then, seven language subsets are defined in domains, which are negative big (NB), negative normal (NM), negative small (NS), zero (Z), positive small (PS), positive normal (PN), and positive big (PB). The membership function is triangle function and defined as Fig. 27. Then, there will be 49 fuzzy rules, and four rules at most will be activated by a certain group of inputs.

According to the different combination of e and de/dt, the fuzzy controller outputs the corresponding ΔK_p and ΔK_i through fuzzy reasoning, so as to achieve the desired control effect. Fuzzy rules have the following four points:

(1) When e is large, in order to improve the response speed of the controller, the larger K_p should be selected. Meanwhile, K_i should be set to zero to prevent system overshoot.

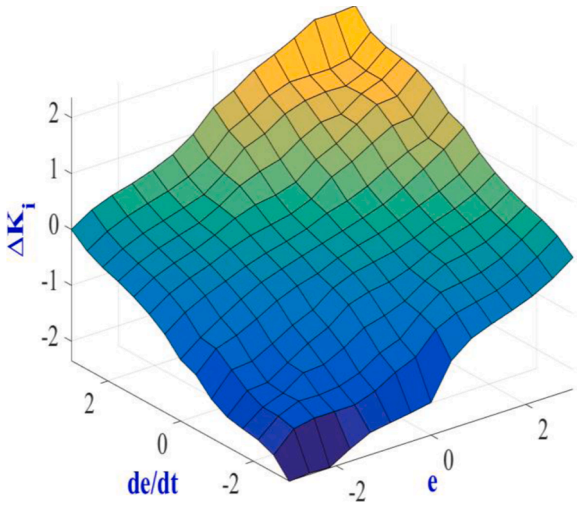

Fig. 29. The change in ΔK_i with e and de/dt.

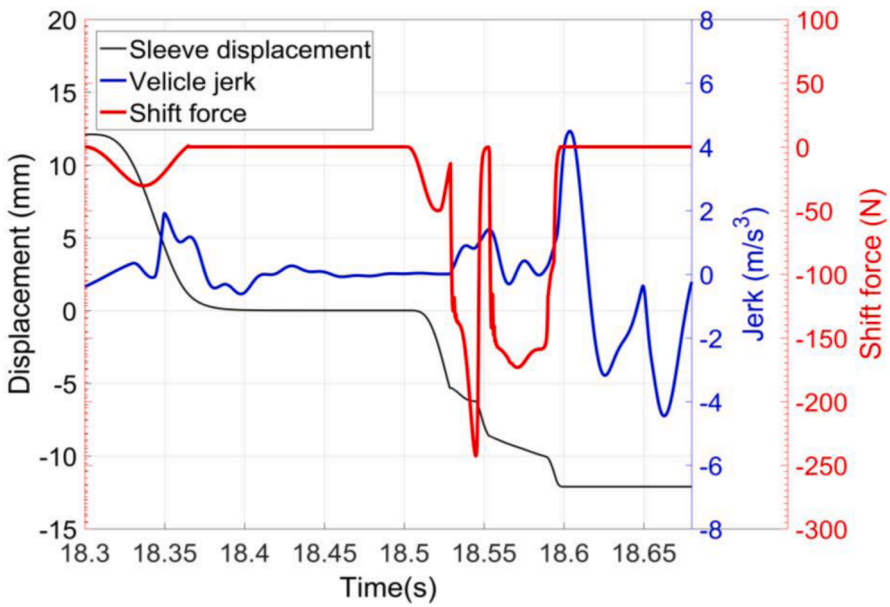

Fig. 30. Shift performance of dual-closed loop fuzzy PI controller.

(2) When e and de/dt are of medium size, the smaller K_p should be selected to prevent system overshoot. Meanwhile, in order to improve the response speed of the system, the medium size K_i should be selected.
(3) When e is small, in order to ensure the stability of the control system, the larger K_p and K_i should be selected.
(4) When de/dt is large, K_p should be appropriately decreased and K_i should be appropriately increased.

In conclusion, fuzzy control rule tables of ΔK_p and ΔK_i can be established according to the setting rules of K_p and K_i, as shown in Tables 7 and 8. Then Figs. 28 and 29 show how ΔK_p and ΔK_i change with e and de/dt, respectively.

The dual-closed loop fuzzy PI controller is used in the model, and the simulation results are shown in the Fig. 30. Compared with the double closed-loop PI control, which can only control the shift force through fixed control parameters, the fuzzy double closed-loop control can control the shift force by changing control parameters in real time according to the actual displacement and velocity of the sleeve. Variable control parameters can further reduce the velocity before the sleeve collides with the guide ring, the dog gear or the limiting device, according to the established fuzzy rules. As a result, the maximum vehicle jerk can reduce to 4.4855 m/s^3, as shown in the Fig. 30.

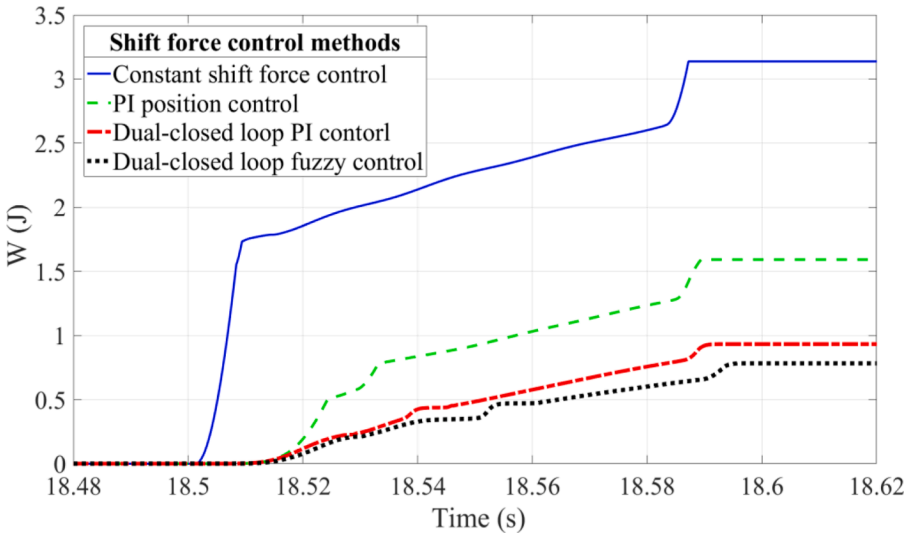

Fig. 31. The work (W) done under different shift force control methods.

Table 9
Control parameters of different shift force control methods.

	Constant shift force control	PI position control	Dual-closed loop PI control	Dual-closed loop fuzzy PI control
Shift force (N)	250	Variable	Variable	Variable
K_{po} (outer)	–	120	0.066	$0.05 + \Delta K_p$
K_{io} (outer)	–	0.029	0.001	$0.001 + \Delta K_i$
K_{pi} (inner)	–	–	2000	2000
K_{ii} (inner)	–	–	0.1	0.1

Table 10
Shift quality under different shift force control methods.

	Constant shift force control	PI position control	Dual-closed loop PI control	Dual-closed loop fuzzy PI control
t_s (s)	0.0868	0.0888	0.0934	0.0962
$\lvert j_v \rvert_{max}$ (m/s^3)	6.0816	5.7207	5.1814	4.4855
W (J)	3.1340	1.5774	0.9282	0.8063

5.5. Comparison

In this section, a new index, which is shift motor energy consumption (W), is proposed. W refers to the work done to push the sleeve from the neutral position to the engaging position, as follows:

$$W = \int (F_a \cdot v) dt \tag{30}$$

where v is the axial velocity of the sleeve, t denotes the time. Fig. 31 shows the shift motor energy consumption under different shift force control methods.

Some control parameters of above different shift force control methods are listed in Table 9. Then the Table 10 shows the results of different shift force control methods. From Table 10, it can be found that with the improvement of the shift force control method, both the vehicle jerk (j_v) and the shift motor energy consumption (W) have decreased significantly, whereas the engaging time (t_s) increases slightly. Hence, it can be concluded that the improvement of shift force control method can effectively improve the shift quality.

6. Conclusions

This paper analyzes the specific structure and working process of a spring-based synchronizer, and establish a two-speed AMT vehicle dynamic model and shifting control model in the AMESim and MATLAB/Simulink environment, based on the traditional synchronizer and the proposed synchronizer, respectively. On the premise of the same parameters, for example, the rotary inertia of

EM, the speed difference and the shift force, the simulation results are analyzed and compared. The results show that the shift quality of the spring-based synchronizer is better than that of the traditional synchronizer. Then, for the spring-based synchronizer, the influences of spring stiffness, speed difference, rotary inertia of EM and shift force on shift quality are analyzed. The analysis results provide a good theoretical basis for the further design and optimization of the novel spring-based synchronizer. Finally, several shift force control methods are proposed, and the influences of different control methods on shift quality is analyzed, which further improves the shift quality. In the follow-up study, the optimization of EM torque reduction and recovery curve will be considered, so as to further reducing the shifting shock.

Declaration of Competing Interest

The authors declare no conflict of interest.

Acknowledgments

This research is supported in part by Fundamental Research Funds for the Central Universities (JZ2019HGPA0100), National Key Research and Development Program of China (2018YFB0105505-03), and Anhui New Energy Automobile and Intelligent Networking Automotive Industry Technology Innovation Project.

References

[1] Y. Wang, E. Lu, H. Lu, N. Zhang, X. Zhou, Comprehensive design and optimization of an electric vehicle powertrain equipped with a two-speed dual-clutch transmission, Adv. Mech. Eng. 9 (1) (2017) 1–29.
[2] C. Tseng, C. Yu, Advanced shifting control of synchronizer mechanisms for clutchless automatic manual transmission in an electric vehicle, Mech. Mach. Theory 84 (2015) 37–56.
[3] W. Mo, J. Wu, P.D. Walker, N. Zhang, Shift characteristics of a bilateral Harpoon-shift synchronizer for electric vehicles equipped with clutchless AMTs, Mech. Syst. Signal Process. 148 (2021), 107166.
[4] S. Aldo, L.P. Gabriele, V. Fabio, B. Stefano, E. Mike, B. Rob, M. Ian, A novel seamless 2-speed transmission system for electric vehicles: principles and Simulation Results, SAE Int. J. Engines 4 (2) (2011) 2671–2685.
[5] H.D. Lee, S.K. Sul, H.S. Cho, J.M. Lee, Advanced gear-shifting and clutching strategy for a parallel-hybrid vehicle, IEEE Ind. Appl. Mag. 6 (6) (2000) 26–32.
[6] X. Zhou, P.D. Walker, J. Ruan, N. Zhang, B. Zhu, Numerical and experimental investigation of drag torque in a two-speed dual clutch transmission, Mech. Mach. Theory 79 (2014) 46–63.
[7] P.D. Walker, B. Zhu, N. Zhang, Powertrain dynamics and control of a two speed dual clutch transmission for electric vehicles, Mech. Syst. Signal Process. 85 (2017) 1–15.
[8] C.H. Yu, C.Y. Tseng, C.P. Wang, Smooth gear-change control for EV clutchless automatic manual transmission, in: Proceedings of the IEEE/ASME International Conference on Advanced Intelligent Mechatronics, IEEE, 2012, pp. 971–976.
[9] F.D. Nicola, A. Sorniotti, T. Holdstock, F. Viotto, Bertolotto S, Optimization of a multiple-speed transmission for downsizing the motor of a fully electric vehicle, SAE Int. J. Altern. Powertrains 1 (1) (2012) 134–143.
[10] H. Zhao, C. Liu, Z. Song, J. Yu, Analytical modeling and comparison of two consequent-pole magnetic-geared machines for hybrid electric vehicles, Energies 12 (10) (2019) 1888.
[11] X. Zhu, Z. Hui, J. Xi, J. Wang, Z. Fang, Optimal speed synchronization control for clutchless AMT systems in electric vehicles with preview actions, in: Proceedings of the American Control Conference, IEEE, 2014, pp. 4611–4616.
[12] W. Mo, P.D. Walker, Y. Tian, N. Zhang, Dynamic analysis of unilateral Harpoon-shift synchronizer for electric vehicles, Mech. Mach. Theory 157 (2021), 104173.
[13] P.D. Walker, N. Zhang, Engagement and control of synchronizer mechanisms in dual clutch transmissions, Mech. Syst. Signal Process. 26 (2011) 320–332.
[14] C. Liu, K. He, L. Li, X. Wang, Y. Liu, Position and force switching control for gear engagement of automated manual transmission gear-shift process, J. Dyn. Syst. Meas. Control 140 (8) (2018), 081010.
[15] Q. Liang, N. Tang, B. Gao, H. Chen, The seamless gear shifting control for pure electric vehicle with 2-speed inverse-AMT, IFAC Proc. Vol. 46 (21) (2013) 507–511.
[16] H. Li, T. Lu, J. Zhang, H. Hao, Modeling and analysis of the synchronization process for a wet dual-clutch transmission, Proce. Inst. Mech. Eng. Part D J. Automob. Eng. 229 (14) (2015) 1981–1995.
[17] S. Kim, J. Park, J. Hong, M. Lee, H. Sim, Transient control strategy of hybrid electric vehicle during mode change, in: Proceedings of the SAE World Congress & Exhibition, SAE International, 2009. -01-0228.
[18] A. Sandooja, Double indexing synchronizer – to amplify the synchronizer capacity, in: Proceedings of the SAE Commercial Vehicle Engineering Congress, SAE International, 2012. -01-2003.
[19] H. Chen, G. Tian, Modeling and analysis of engaging process of automated mechanical transmissions, Multibody Syst. Dyn. 37 (4) (2016) 345–369.
[20] H. He, Z. Liu, L. Zhu, X. Liu, Dynamic coordinated shifting control of automated mechanical transmissions without a clutch in a plug-in hybrid electric vehicle, Energies 5 (8) (2012) 3094–3109. Inventi Impact Vehicular Technology.
[21] B. Li, W. Ge, X. Yu, S. Shao, H. Liu, Innovative design and gearshift control for direct-drive electromagnetic gearshift system equipped with servo synchronizer, Proc. Inst. Mech. Eng. Part D J. Automob. Eng. 233 (5) (2019) 1115–1124.
[22] H. Yu, J. Xi, F. Zhang, Y. Hu, H.R. Karimi, Research on gear shifting process without disengaging clutch for a parallel hybrid electric vehicle equipped with AMT, Math. Probl. Eng. (6) (2014) 1–12.
[23] H. Wu, Z. Zhong, Z. Yu, X. Wang, X. Chen, Shifting control of a novel active transmission for hybrid vehicle without the use of clutch, in: Proceedings of the IEEE Conference and Expo Transportation Electrification Asia-Pacific (ITEC Asia-Pacific), 2014, pp. 1–4.
[24] C.H. Yu, C. Yow, Tseng, Research on gear-change control technology for the clutchless automatic-manual transmission of an electric vehicle, Proc. Inst. Mech. Eng. Part D J. Automob. Eng. 227 (10) (2013) 1446–1458.
[25] X. Zhu, H. Zhang, J. Xi, J. Wang, Z. Fang, Robust speed synchronization control for clutchless automated manual transmission systems in electric vehicles, Proc. Inst.Mech. Eng. Part D J. Automob. Eng. 229 (4) (2015) 424–436.
[26] A. Mohammadzadeh, S. Ghaemi, O. Kaynak, S.K. Mohammadi, Robust predictive synchronization of uncertain fractional-order time-delayed chaotic systems, Soft Comput. 23 (16) (2019) 6883–6898.
[27] S. Yahagi, I. Kajiwara, T. Shimozawa, Slip control during inertia phase of clutch-to-clutch shift using model-free self-tuning proportional-integral-derivative control, Proc. Inst. Mech. Eng. Part D J. Automob. Eng. 234 (9) (2020) 2279–2290.

[28] H. Liu, Y. Lei, Z. Li, J. Zhang, Y. Li, Gear-shift strategy for a clutchless automated manual transmission in battery electric vehicles, SAE Int. J.Commer. Veh. 5 (1) (2012) 57–62.
[29] J. Liang, H. Yang, J. Wu, N. Zhang, P.D. Walker, Power-on shifting in dual input clutchless power-shifting transmission for electric vehicles, Mech. Mach. Theory 121 (2018) 487–501.
[30] P.D. Walker, Y. Fang, N. Zhang, Dynamics and Control of clutchless automated manual transmissions for electric vehicles, J. Vib. Acoust. 139 (6) (2017) 1–13.